Large-scale current systems and ground magnetic disturbance during deep substorm injections

J. Yang,[1] F. R. Toffoletto,[1] R. A. Wolf,[1] S. Sazykin,[1] P. A. Ontiveros,[1,2] and J. M. Weygand[3]

Received 27 November 2011; revised 7 March 2012; accepted 11 March 2012; published 25 April 2012.

[1] We present a detailed analysis of the large-scale current systems and their effects on the ground magnetic field disturbance for an idealized substorm event simulated with the equilibrium version of the Rice Convection Model. The objective of this study is to evaluate how well the bubble-injection picture can account for some classic features of the substorm expansion phase. The entropy depletion inside the bubble is intentionally designed to be so severe that it can penetrate deep into geosynchronous orbit. The results are summarized as follows: (1) Both the region-1-sense and region-2-sense field-aligned currents (FACs) intensify substantially. The former resembles the substorm current wedge and flows along the eastern and western edges of the bubble. The latter is connected to the enhanced partial ring current in the magnetosphere associated with a dipolarization front earthward of the bubble. In the ionosphere, these two pairs of FACs are mostly interconnected via Pedersen currents. (2) The horizontal ionospheric currents show a significant westward electrojet peaked at the equatorward edge of the footprint of the bubble. The estimated ground magnetic disturbance is consistent with the typical features at various locations relative to the center of the westward electrojet. (3) A prominent Harang-reversal-like boundary is seen in both ground ΔH disturbance and plasma flow pattern, appearing in the westward portion of the equatorward edge of the bubble footprint, with a latitudinal extent of $\sim 5^\circ$ and a longitudinal extent of the half width of the bubble. (4) The dramatic dipolarization inside the bubble causes the ionospheric map of the inner plasma sheet to exhibit a bulge-like structure, which may be related to auroral poleward expansion. (5) The remarkable appearance of the westward electrojet, Harang-reversal-like boundary and poleward expansion starts when the bubble reaches the magnetic transition region from tail-like to dipole-like configuration. We also estimate the horizontal and vertical currents using magnetograms at tens of ground stations for a deep injection substorm event occurred on April 9, 2008, resulting in a picture that is qualitatively consistent with the simulation. Based on the simulations and the observations, an overall picture of the ionospheric dynamics and its magnetospheric drivers during deep bubble injections is obtained.

Citation: Yang, J., F. R. Toffoletto, R. A. Wolf, S. Sazykin, P. A. Ontiveros, and J. M. Weygand (2012), Large-scale current systems and ground magnetic disturbance during deep substorm injections, *J. Geophys. Res.*, *117*, A04223, doi:10.1029/2011JA017415.

1. Introduction

[2] The magnetic field reconfiguration in the magnetosphere and the magnetic disturbance on the ground during substorm expansions can be very complicated. Their variations are usually explained by analyzing the formation and decay of large-scale current systems. One well-known system in the magnetosphere is the substorm current wedge (SCW) [*McPherron et al.*, 1973], which involves bundles of flux tubes carrying downward field-aligned currents (FACs) eastward of upward ones. Many studies have attributed the major magnetic dipolarization during substorm expansions to the SCW, as it partially disrupts the cross-tail currents [e.g., *Nagai*, 1982; *Hesse and Birn*, 1991]. It is also widely accepted that a significantly enhanced westward electrojet forms around the ionospheric onset sector, which is inferred by analyzing ground magnetograms [e.g., *Akasofu et al.* 1965; *Clauer and McPherron*, 1974]. Although the

[1]Department of Physics and Astronomy, Rice University, Houston, Texas, USA.
[2]Now at Shell Exploration and Production Company, Houston, Texas, USA.
[3]Institute of Geophysics and Planetary Physics, University of California, Los Angeles, California, USA.

0148-0227/12/2011JA017415

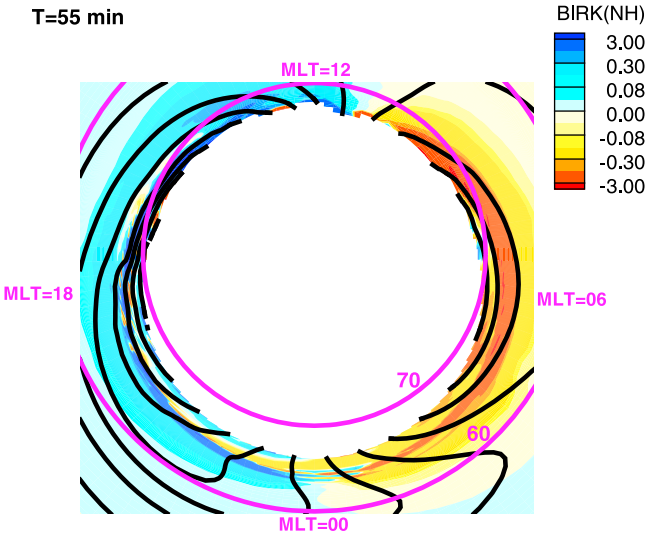

Figure 1. Ionospheric Birkeland currents and potential pattern at the end of the growth phase. Birkeland current is in units of $\mu A/m^2$. Positive (blue) current is down into the ionosphere, negative (red) up. The Sun is to the top. Equipotentials are separated by 8 kV.

scientific community has reached consensus on some typical features of substorms (e.g., auroral morphology [*Akasofu*, 1964]; ground magnetograms [*Rostoker et al.*, 1980]), a comprehensive picture of currents, electric fields and plasma flows in the ionosphere, their ground effects and their magnetospheric drivers remains a matter of much debate because of the variability and highly dynamic nature of substorms and because of limited coverage of observations.

[3] Numerical simulations of the coupled magnetosphere-ionosphere system have the advantage of providing a global view, and a long-term effort in that direction has been made using the Rice Convection Model (RCM) and its derivative versions [*Harel et al.*, 1981; *Toffoletto et al.*, 2003]. Some recent work with RCM-related models [*Toffoletto et al.*, 2000; *Zhang et al.*, 2008; *Zhang et al.*, 2009, *Yang et al.*, 2011a] has pursued the idea that substorm injections from the main plasma sheet to the inner magnetosphere consist of earthward-propagating bubbles, which contain lower $PV^{5/3}$ flux tubes than the background [*Pontius and Wolf*, 1990]. The quantity $PV^{5/3}$ is called the entropy parameter (or entropy for simplicity in this paper), where P is the plasma pressure and $V = \int ds/B$ is the flux tube volume per unit magnetic flux. Increasingly, studies have shown that plasma sheet bubbles and the bursty bulk flows (BBFs) are essentially the same thing [e.g., *Sergeev et al.*, 1996; *Chen and Wolf*, 1999; *Runov et al.*, 2009; *Birn et al.*, 2009].

[4] In this study, we will qualitatively test numerical simulation results of a bubble injection against typical and classic features observed during a substorm expansion phase; we will also provide large-scale electromagnetic dynamics for deep injections obtained from both simulations and observations. The idealized bubble injection event we will analyze was previously modeled by *Yang et al.* [2011a] (hereafter referred to as Paper 1) using the equilibrium version of the RCM (RCM-E), though the discussion there primarily focused on the ion acceleration in the magnetosphere. In section 2 of this paper, we will analyze the simulation results in detail and investigate the electric currents and their induced dynamics both in the ionosphere and on the ground for one particular type of substorm that is accompanied by a deep injection. In section 3, we will present an example that supports our model predictions for the same type of injection event. We finally synthesize the modeled electric fields, plasma flows, currents and ground magnetometers in the ionosphere and their associated magnetospheric driver in section 4.

2. RCM-E Simulation Results

[5] We only briefly summarize the simulation setup here as a detailed description of the model and the initial and boundary conditions can be found in Paper 1, along with a description of the strengths and limitations of using the RCM-E for bubble injection simulations. The idealized event consists of the substorm growth phase and expansion phase. The growth phase simulation lasts 55 min, in which the initial and boundary conditions are set according to empirical models driven by steady solar wind conditions. The expansion phase is modeled by placing a depleted plasma sheet bubble along a sector centered at midnight with a fixed width of 2 h in local time in the ionosphere. Due to the dramatic magnetic field collapse during the bubble injection, the spatial extent of the bubble in the Y direction along the tailward boundary in the equatorial plane is not constant in time, but decreases from $\sim$5 R_E at T = 55 min to $\sim$2 R_E at T = 70 min. *Nakamura et al.* [2004] estimated the width of flow channels observed by Cluster tailward of 15 R_E and obtained the statistical average as 2–3 R_E in the dusk-dawn direction. Our simulation shows that the bubble tends to spread toward the dusk and dawn directions as it moves closer to the Earth due to larger gradient/curvature drifts and vortex-like flow patterns (e.g., see Figure 7a in Paper 1), which implies that the flow channel inside 15 R_E should be even wider than *Nakamura et al.*'s estimation. Therefore, the width of the bubble along the tailward boundary in our simulation is reasonable compared with typical values inferred from observations. The value of $PV^{5/3}$ at midnight is reduced from 0.30 nPa$(R_E/nT)^{5/3}$ at the end of the growth phase to 0.05 nPa$(R_E/nT)^{5/3}$ within 5 min, and it remains at this value afterward. The cross polar cap potential drop is set at a constant value of 100 kV throughout the simulation. The ionospheric conductances are estimated from the IRI-90 (International Reference Ionosphere) model plus enhancement due to electron precipitation, which is assumed to be at 1/3 of the strong-pitch angle scattering limit. The model assumes zero dipole tilt, and field-aligned potential drops are neglected.

[6] Figure 1 shows the ionospheric potential and Birkeland pattern in the growth phase, just before the launch of the bubble. Well developed region-2 currents (up on the dawn side, down at dusk) partly shield the lower latitudes from the strong, growth-phase convection electric field. As is usual in conventional RCM calculations [*Harel et al.*, 1981], the region-1 currents lie in the white region, poleward of the RCM boundary. Large-scale region-1 currents appear within the RCM modeling region if and only if the boundary-condition $PV^{5/3}$ is larger on the flanks than in the midnight region [*Karty et al.*, 1984; *Yang et al.*, 1994].

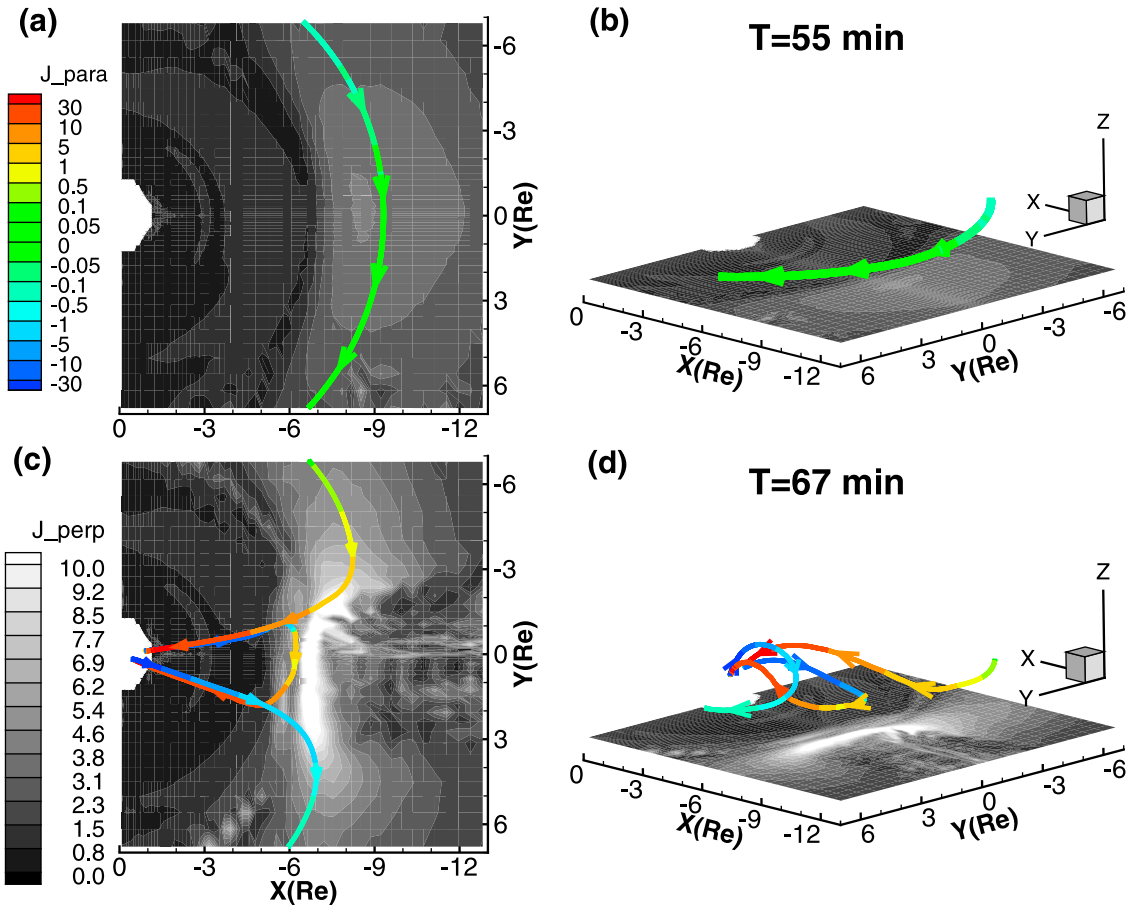

Figure 2. Top view of current density (in units of nA/m^2) perpendicular to the magnetic field in the equatorial plane (gray contours) and the electric current line flowing through X = −7.56, Y = −5.58 and Z = 1.24 R_E at (a) T = 55 min and (c) T = 67 min. The color scales represent the current density (in units of nA/m^2) parallel to the magnetic field. The red/yellow and blue/cyan colors represent field aligned currents down to and up from the ionosphere. (b and d) Side view of Figures 2a and 2c, respectively.

The values we assume for the boundary $PV^{5/3}$ distribution in present case have a broad maximum near midnight, so we are implicitly assuming that the region-1 currents lie poleward of our boundary during the growth phase. The electric field distribution does not suggest a strong electric field Harang discontinuity in the auroral zone near midnight, but with a reversal in the meridional electric field, which changes sign at subauroral latitudes. Earlier RCM simulations have suggested two physical mechanisms for the Harang discontinuity: (1) penetration of low-energy plasma sheet-ions significantly earthward of the more energetic ions [*Harel et al.*, 1981], creating a band of upward current poleward of the downward region-2 current in the pre-midnight sector; this process has recently been studied in considerable quantitative detail by *Gkioulidou et al.* [2009]; (2) higher boundary $PV^{5/3}$ on the dusk side than on the dawn side [*Erickson et al.*, 1991]. The boundary condition used for the present run did not allow mechanism 2 to operate. Mechanism 1 created a band of upward current before midnight, but it was not strong enough to produce a Harang structure in the growth phase. The focus of this paper is not on currents and electric fields in the growth phase, but rather on the major changes that occur in Birkeland currents and electric fields at the nightside during the expansion phase, due to the injection of a deep penetrating bubble.

2.1. Large-Scale Current Systems in the Magnetosphere

[7] Figure 2 compares representative electric current flowing through a fixed point (X = −7.56, Y = −5.58 and Z = 1.24 R_E) at T = 55 min, when the bubble is just about to be launched on the tailward boundary, with that at T = 67 min when the bubble injection has just reached inside geosynchronous orbit. Before the bubble injection, the equatorial current system is smoothly distributed in the plasma sheet with a peak value of $J_\perp \approx 4$ nA/m^2 at X ≈ −8.5 R_E. The green color on the westward electric current flow line indicates that the current is mostly perpendicular. During the bubble injection, the nightside magnetosphere exhibits two intense current systems with opposite sense. At higher latitudes, the westward electric current in the post-midnight sector (Y < −3 R_E) is diverted along field lines to the ionosphere. In the pre-midnight sector, the FACs flow from the ionosphere to the magnetosphere and connect back to the westward currents near the equatorial plane (Y > 3 R_E). The topology of this

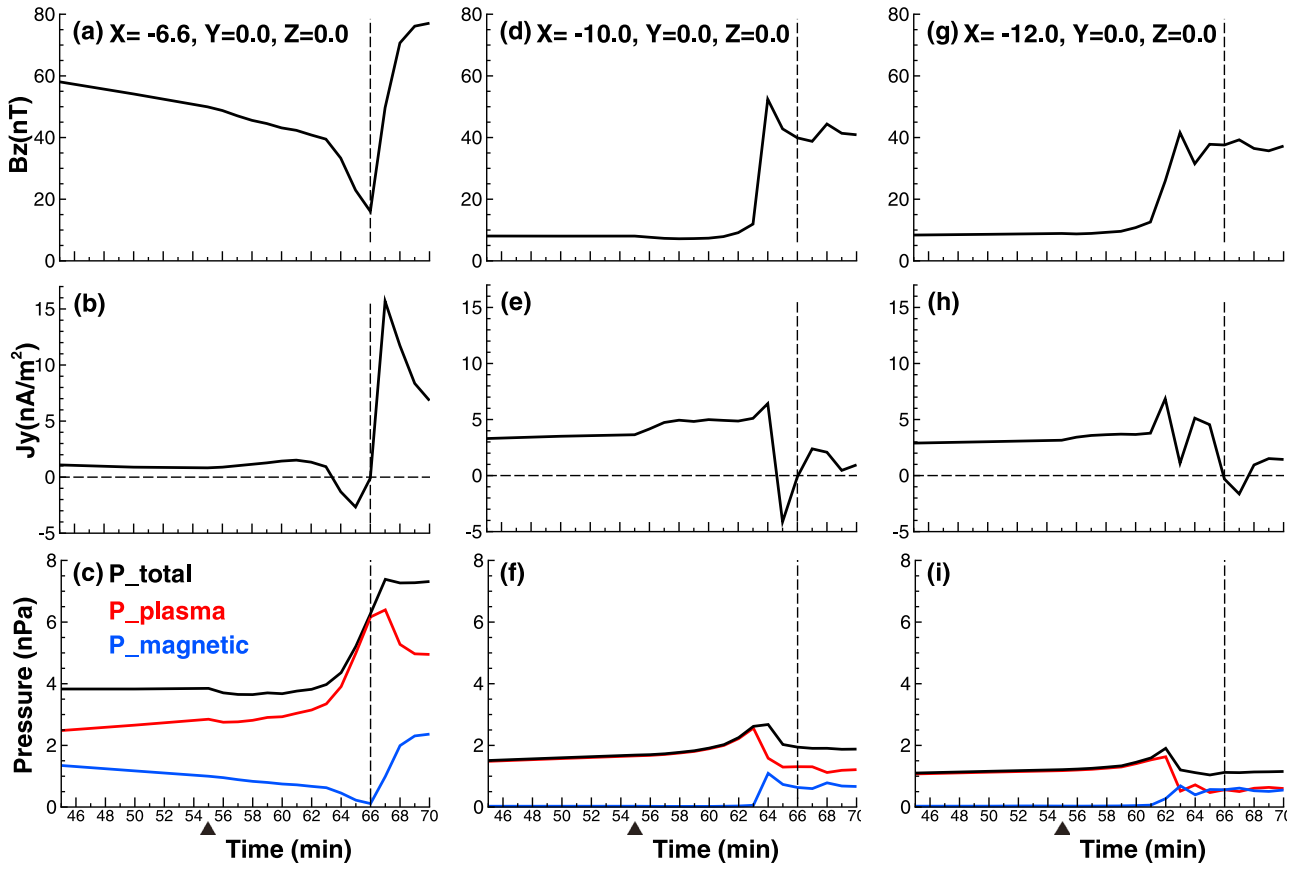

Figure 3. From top to bottom are B_Z, J_Y and plasma pressure (red), magnetic pressure (blue) and total pressure (black) at locations $X = -6.6$, -10.0 and -12.0 R_E (from left to right) and $Y = Z = 0$ R_E. The triangles and the dashed lines represent T = 55 and T = 66 min, respectively.

current loop clearly resembles the SCW, which is region-1-sense. At lower latitudes, a strengthened region-2-sense FAC system appears. This current system involves upward flow from the ionosphere into the magnetosphere in the post-midnight sector and connects to a westward current around the equatorial plane. It is finally diverted back to the FACs again from the magnetosphere into the ionosphere but in the pre-midnight sector. It is worth noting that, for a representative current flow line, Figure 2c suggests that the upward-and-downward pair of FACs either for the SCW or for the region-2-sense do not close themselves primarily by longitudinal currents in the ionosphere; rather that the upward and downward FACs at the same MLTs are interconnected through latitudinal Pedersen currents in ionosphere (see section 2.2 for details). The gray colors in the equatorial plane clearly show that the cross-tail current is partially disrupted tailward of X~-7 R_E; while the partial ring current is significantly enhanced between X~-5 and X~-7 R_E, with its dusk-to-dawn width approximately the same as the width of the FAC wedges.

[8] In the context of the RCM-E, the inertial effects are neglected and the flows are assumed to be slow compared with MHD waves, thus the role of shear Alfvénic waves in FAC generation [*Southwood and Kivelson*, 1991; *Song and Lysak*, 2001] is neglected. Under the quasi-static assumption, the FACs in the closed field line region are generated by plasma pressure gradients between adjacent flux tubes [*Vasyliunas*, 1970] and are closed primarily by Pedersen currents in the ionosphere. Therefore, the strong region-1-sense SCW appears along the western and eastern edges of the bubble, inside of which severe depletion is imposed through the tailward boundary conditions. The formation of SCW can also be explained in terms of plasma drift. The under-populated flux tubes inside the bubble carry less gradient/curvature drift currents than those outside of them and thus the westward cross-tail currents are partially disrupted. In order to maintain current conservation, the disruption has to be compensated by the FACs. On the other hand, because the earthward rush of the bubble injected near midnight dents the inner edge of the plasma sheet inward in that local-time sector, locally enhanced westward currents appear earthward of the bubble (bright region in Figure 2c). The co-existence of the region-1-sense and region-2-sense FACs that are directly induced by the intrusion of the bubble are modeled self-consistently with the RCM-E. Similar results are also shown in a bubble injection simulation using the RCM in which the magnetic field was specified with empirical models rather than being calculated with an equilibrium solver [*Zhang et al.*, 2009].

[9] Figure 3 shows the time sequence of B_Z, J_Y, and pressure at different locations in the equatorial plane. As the bubble propagates inside geosynchronous orbit, the magnetic field there first decreases at a faster rate than during the earlier growth phase, in association with an increase in the

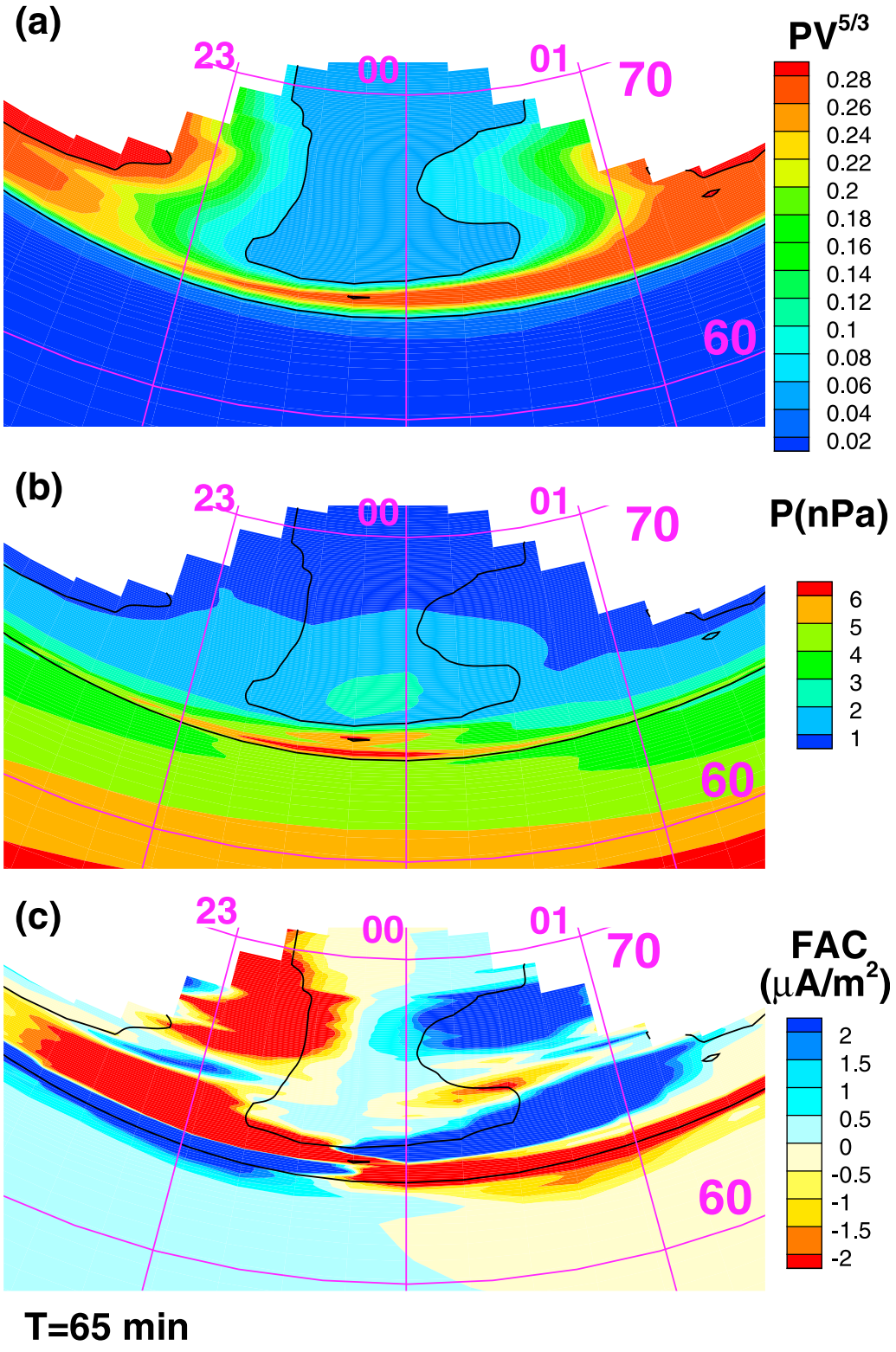

Figure 4. From top to bottom are (a) entropy parameter $PV^{5/3}$ (in units of nPa$(R_E/nT)^{5/3}$), (b) ionospheric map of equatorial plasma pressure and (c) field-aligned current density in color contours (positive is down to the ionosphere). Black lines represent $PV^{5/3}$ contours at values of 0.06 and 0.28. The purple lines represent latitudes (60° and 70°) and MLTs (23, 00 and 01).

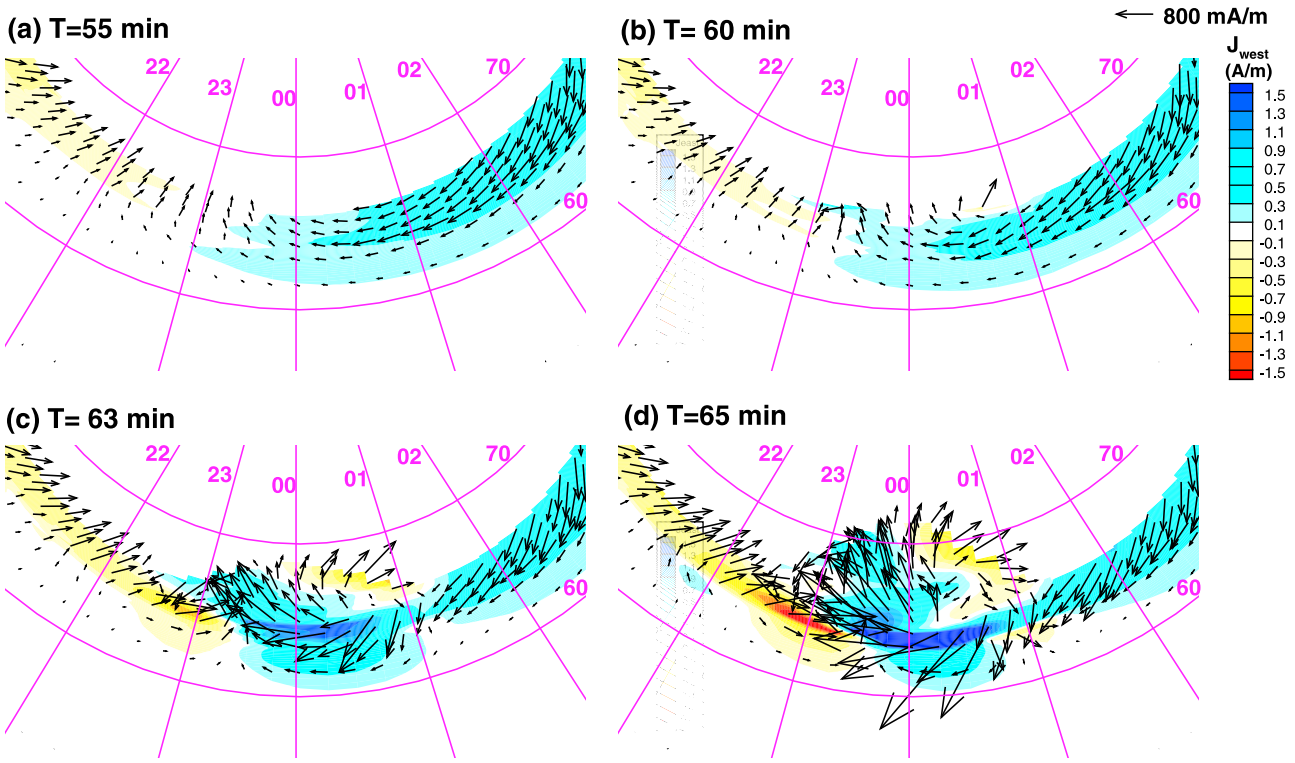

Figure 5. Horizontal current density (black arrows) in the ionosphere and its westward component (color contours) at different times.

plasma pressure (left column of Figure 3). Paper 1 demonstrated that such a diamagnetic effect occurs inside a high-$PV^{5/3}$ region pushed ahead of the bubble, which is suggested as an explanation of the fact that the magnetic field decreases before the arrival of a dipolarization front during some substorm injections [*Sergeev et al.*, 2009; *Runov et al.*, 2009]. On the earthward side of that high entropy structure, the eastward current (Figure 3b) corresponds to a tailward gradient of the plasma pressure (Figure 3c). The geosynchronous magnetic field starts to dipolarize after T = 66 min, when the bubble reaches that location. The peak value of J_Y associated with this sharp dipolarization is ~17 nA/m^2, consistent with the estimated 20 nA/m^2 by *Runov et al.* [2011]. The plasma pressure and J_Y remain enhanced for an extended period, suggesting a strengthened partial ring current inside the head of the bubble. At more tailward locations (middle column of Figure 3 for $X = -10$ R_E and right column of Figure 3 for $X = -12$ R_E), no clear diamagnetic effect (a decrease in B_Z associated with an increase in plasma pressure) is seen, although a gradual plasma pressure buildup is registered at both locations before the major dipolarization. Inside the dipolarization region, the overall magnitude of J_Y is much smaller than during the pre-bubble injection time (Figures 3e and 3h), clearly indicating the partial disruption of the cross-tail current. This disruption is also associated with the plasma pressure decrease due to large depletion of the flux tubes inside the bubble (Figures 3f and 3i). However, the sum of the plasma and the magnetic pressure after the head of the bubble passes is roughly the same as it was before the bubble arrived.

2.2. Large-Scale Current Systems in the Ionosphere

[10] The driver of the co-existing strong region-1-sense and region-2-sense FACs in the magnetosphere is identified as the bubble and the structure ahead of the bubble, respectively (see Figures 5–7 in Paper 1). Figure 4 demonstrates the relationship of the FACs, the $PV^{5/3}$ and the plasma pressure mapped into the ionosphere along the magnetic field lines. The bubble with a width of 2 h in LT moves from higher to lower latitude and pushes a thin layer equatorward. The local maximum of the plasma pressure appears near the earthward edge of the bubble. In Figure 4c, strong region-2-sense FACs map along the equatorward edge of the high $PV^{5/3}$ layer, with the downward FACs forming west of the upward. At T = 65 min, these region-2-sense FACs are as thin as ~1° in latitude, centered at 63°. The overall region-1-sense FACs emerge along the edges of the bubble, with the downward east of the upward from ~64° to ~70°, with an exception of a very thin layer of region-2-sense FACs with a latitudinal width of ~1° centered at ~66°. Theoretically, the FACs at latitudes higher than ~64° should mainly be the region-1-sense SCW (see also cartoon in Figure 14) because they are currents flowing on the edges of the bubble as implied by the Vasyliunas' equation. However, because of the highly distorted magnetic configuration and the fairly strong west-east spreading of the bubble, the actual upward/downward sense of FACs generated by the pressure gradient fluctuates violently. For example, there is one thin layer of region-2-sense FACs centered at ~66°, where the gradient of $PV^{5/3}$ has a predominantly northward component.

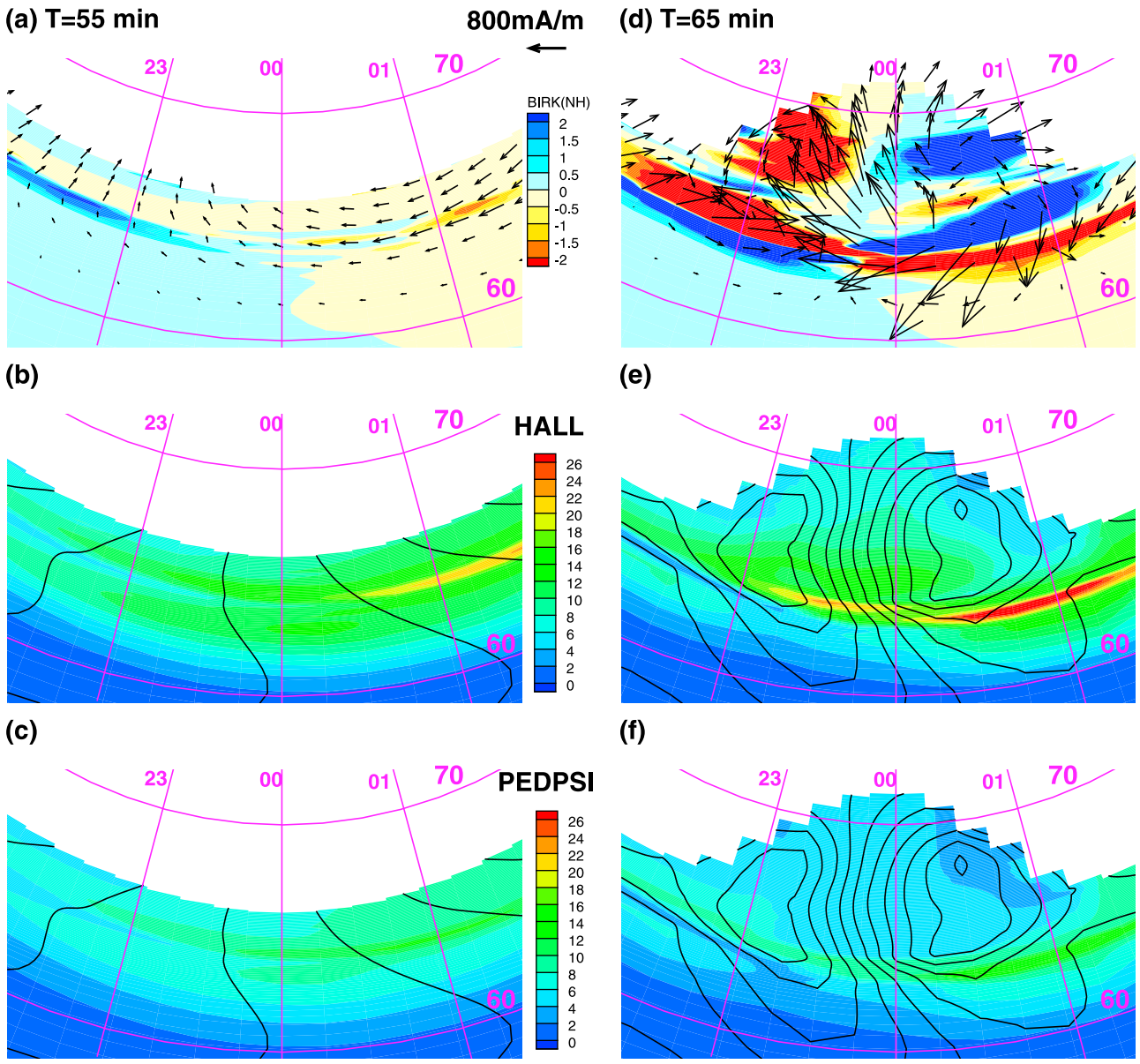

Figure 6. Color contours from top to bottom are field-aligned current density (in units of μA/m^2), Hall and Pedersen conductance per hemisphere at times (left) T = 55 min and (right) T = 65 min. The black arrows in the top row represent horizontal currents. The solid lines in the lower two rows are electric equipotentials every 8 kV.

[11] The overall magnetospheric convection during the growth phase is strong in this run, as the cross polar cap potential drop applied in the RCM simulation region is 100 kV (see Paper 1 for details). Therefore, the ionospheric currents between ~63° and 66° latitude are fairly large with a maximum value of ~600 mA/m in the westward direction east of 23.5 MLT (Figure 5a). The horizontal currents in the ionosphere do not immediately increase dramatically in the first five minutes following the launch of the bubble on the boundary (Figure 5b). Substantial strengthening starts at about T = 63 min (Figure 5c) when the bubble reaches X = -10 R_E (middle column of Figure 3) and further increases at later time (Figure 5d). A strong westward electrojet is peaked in the midnight sector with a latitudinal width of ~2°, but weaker westward ionospheric currents also extend both poleward and equatorward. Thus the total latitudinal width of the westward current is ~10°. The eastward ionospheric current with a width of ~2° in latitude becomes dominant west of the westward electrojet.

[12] Enlarged plot in Figure 6a shows that the FACs mapped inside the RCM-E simulation region are primarily region-2-sense before the bubble injection, with their maximum strength centered at ~64° latitude in the ionosphere and mapped out at r ~ 7.5 R_E in the nightside magnetosphere. Figure 6d shows there are two vortex-like current patterns roughly centered at the westward and eastward edges of the bubble, topologically overlapped with the two vortices in the electric equipotentials in Figure 6e. Comparing the electric field and the conductance before and during the bubble injection, we can conclude that the

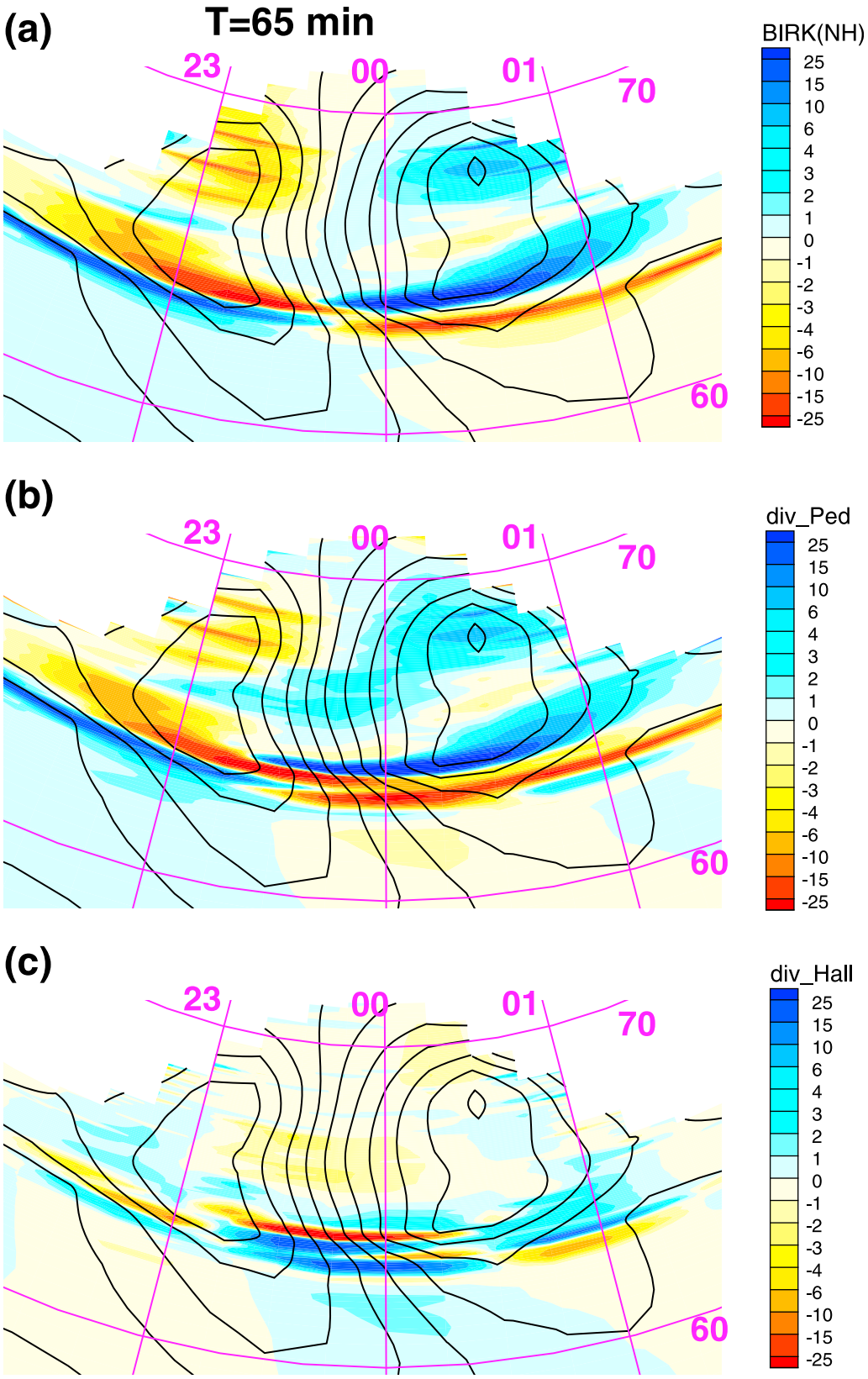

Figure 7. From top to bottom are field-aligned current density, divergence of ionospheric Pedersen currents and divergence of ionospheric Hall currents (in units of $\mu A/m^2$). The black lines are electric equipotentials every 8 kV.

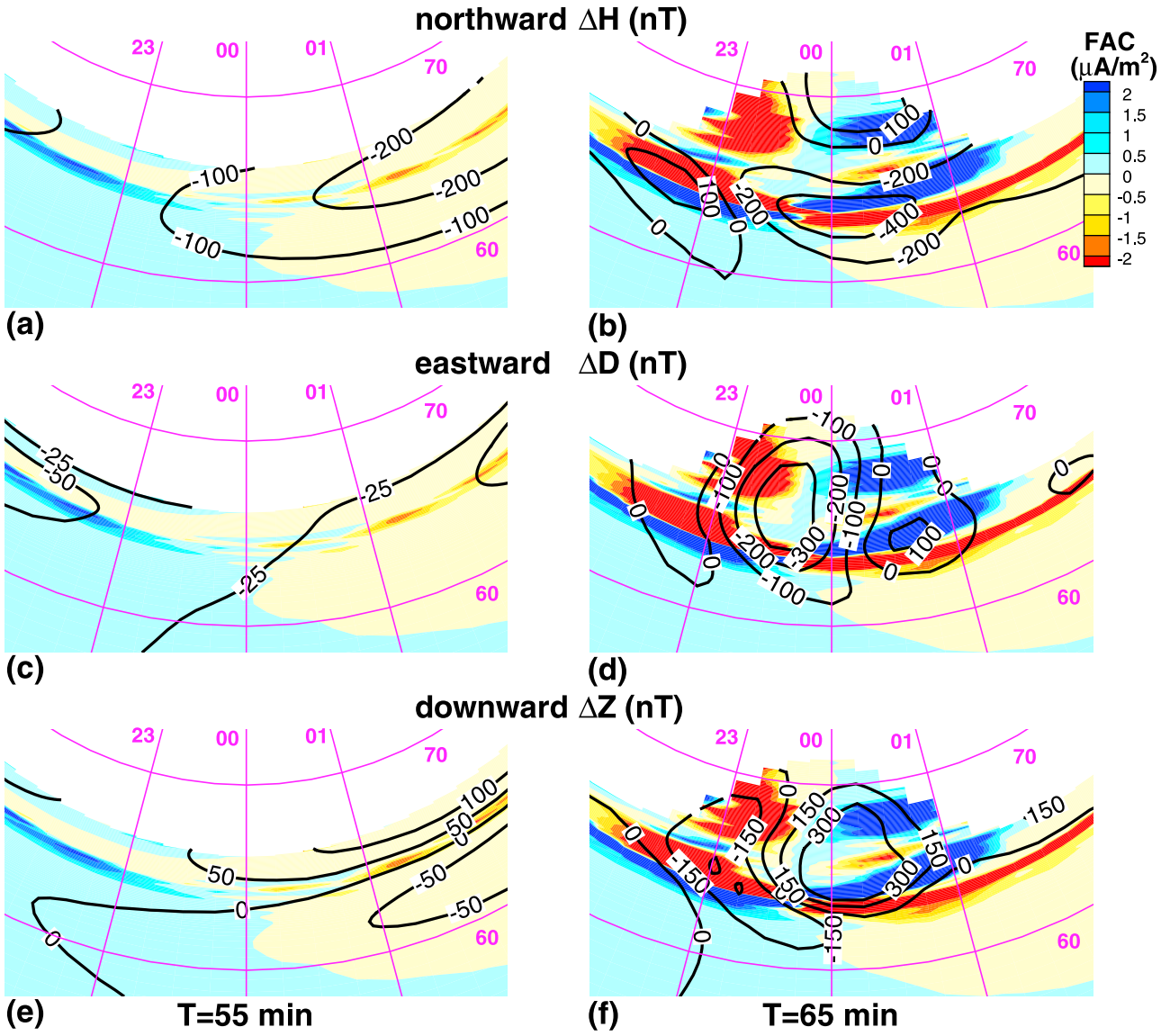

Figure 8. From top to bottom are the northward, eastward and downward components of the calculated ground magnetic disturbance (black line contours) relative to the zero-tilt dipole field. The color contours represent the FAC density. The left and right panels are for T = 55 min and T = 65 min, respectively.

enhancement of the horizontal currents is mainly due to the intensification of the electric field in the ionosphere, which increases by a factor of ~5; while both Hall and Pedersen conductances increase only by a factor of ~2. Overall, the Pedersen conductance is about half magnitude of the Hall conductance in the auroral zone (Figures 6e and 6f), suggesting the Pedersen currents are about half of the Hall currents. However, if we considered field-aligned potential drops and/or Alfven wave heating, the average energy of precipitating particles would go up and the ratio of Pedersen to Hall conductances will be smaller than the results presented here. It is also worth noting that, although the FACs expand as high as ~71° in ionospheric latitude, the conductance in this region is not particularly low. These FACs do not map far out into the tail, because field lines are dipolarized inside the bubble. A more detailed explanation of this bulge-like region will be given in section 2.4.

[13] Figure 6d also suggests that the region-1-sense FACs at high latitudes and the region-2-sense FACs at lower latitudes are interconnected mainly by the meridional Pedersen current. In order to carefully investigate the coupling between the FACs and the horizontal currents, we calculated the divergence of ionospheric Pedersen and Hall current shown in Figure 7. (Note that the color scales in Figure 7 are different from Figure 6d.) The results indicate that the divergence of Hall current has a local minimum (negative values) and a local maximum (positive values) in a region from ~63° to 64° latitude and from ~23.5 to ~00 MLT; while the divergence of Pedersen current is also large but with different signs from the divergence of Hall current. Therefore, a substantial amount of the divergence of Hall and Pedersen current cancel each other and total FAC density is not significant there. In contrast, in the region east of

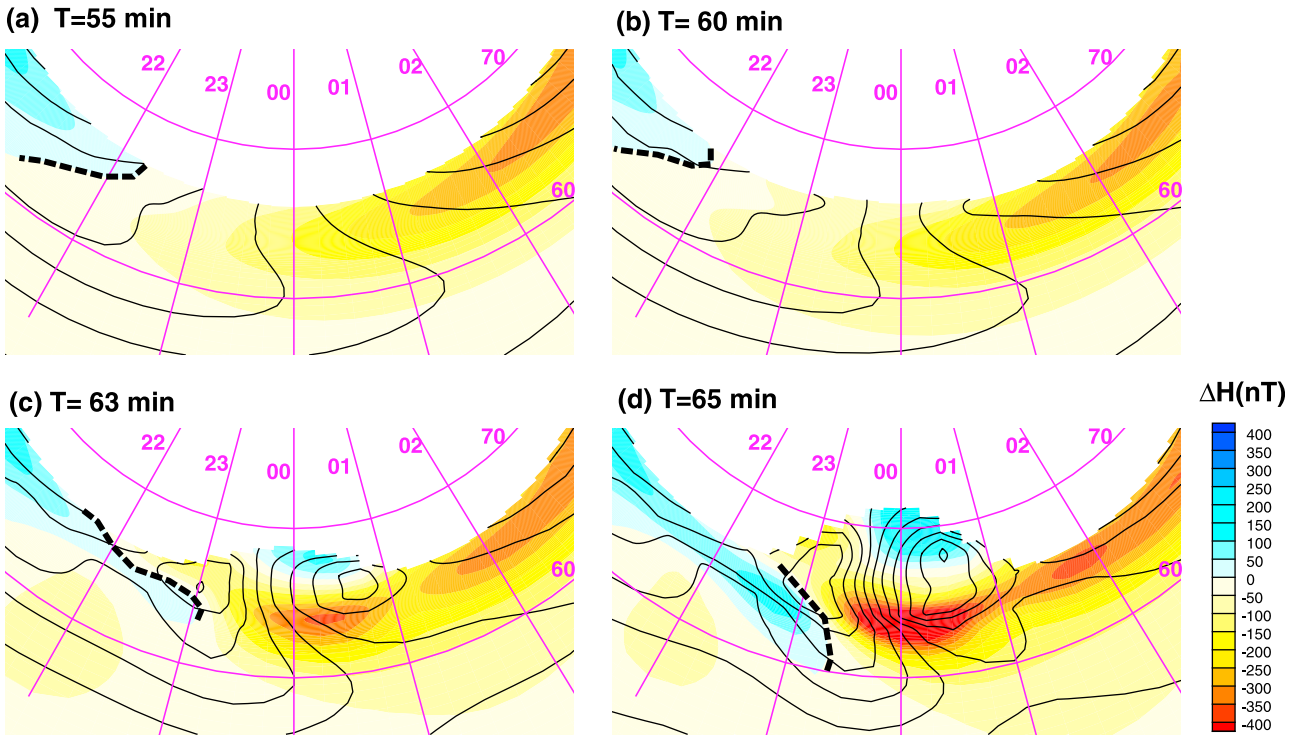

Figure 9. The northward component of the calculated ground magnetic field disturbance (color contours) and electric equipotentials (every 8 kV) at different times. The dashed thick lines represent a segment of the ΔH = 0 nT boundary.

~00 MLT and west of 23.5 MLT at roughly the same latitudes, the absolute value of divergence of Pedersen current is notably larger than the divergence of Hall current, indicating the FACs are mostly coupled with the ionospheric Pedersen current. Figure 7 also shows that a small part of the region-1-sense FACs at higher latitudes (>~65°) are connected mainly by the east-west Pedersen current inside the bubble. Our results are qualitatively consistent with the results reported by *Chen et al.* [1982].

2.3. Ground Magnetic Disturbance

[14] In this section, we will concentrate on the results of the ground magnetic field disturbance calculated by using a synthetic magnetogram code [*Ontiveros*, 2009]. This code assumes that the ground magnetic disturbance is contributed by four large-scale current systems: (1) the ionospheric currents calculated in the RCM; (2) the inner magnetospheric currents in the RCM; (3) currents flowing in the outer magnetosphere and solar wind, the magnetic effects of which can be represented by a scalar potential within the RCM modeling region; and (4) ground induction currents (GICs), which can also be represented by a scalar potential. Earlier applications of the code in storm and Steady Magnetospheric Convection (SMC) events can be found in the works of *Ontiveros* [2009] and *Yang et al.* [2010], respectively.

[15] Figure 8 depicts the ground magnetic disturbance relative to the untilted dipole field in three directions before and during the bubble injection. Due to the fairly large westward currents (Figure 6a), the northward magnetic field disturbance ΔH is mainly negative (Figure 8a) and the downward disturbance ΔZ is positive poleward of that current system and negative equatorward of it (Figure 8e). At T = 65 min, the ΔH component becomes strongly negative eastward of ~23.5 MLT with a peak of ~−500 nT centered near the midnight at 64° latitude (Figure 8b) due to the intensified westward electrojet (Figure 6d). The ΔH also shows positive excursion west of ~23.5 MLT because of the northeast ionospheric currents overhead. The westward ΔD emerges for most of the region inside the bubble and extends equatorward of the center of westward electrojet in the midnight and pre-midnight sector. The eastward ΔD only shows up around the eastward and westward edges of the bubble where the ionospheric currents have an equatorward component. The ΔZ is mainly downward in the region eastward of ~23.5 MLT; while it is upward along the westward edge of the bubble and also extends equatorward of the center of the westward electrojet.

[16] Figure 9 shows a wider view of the time evolution of the ΔH component. Similar to Figure 5, in the first five minutes of the injection, there is hardly any change in ΔH. The reason is that the ground magnetic disturbance (except for pulsations due to waves, which are not modeled in the RCM-E) at 60–70° latitude is mainly caused by horizontal ionospheric currents and the GICs, whose changes during this period are subtle. However, starting from approximately T = 63 min, the ΔH = 0 boundary moves toward the sector where the bubble is injected. At T = 65 min, the gradient of ΔH along the ΔH = 0 boundary increases significantly, which indicates a prominent appearance of a magnetically defined Harang discontinuity/reversal [*Harang*, 1946; *Heppner*, 1972]. This northwest-to-southeast-aligned Harang-reversal-like structure extends from ~22.5 MLT and ~66° latitude to ~23.5 MLT and ~60° latitude along the westward

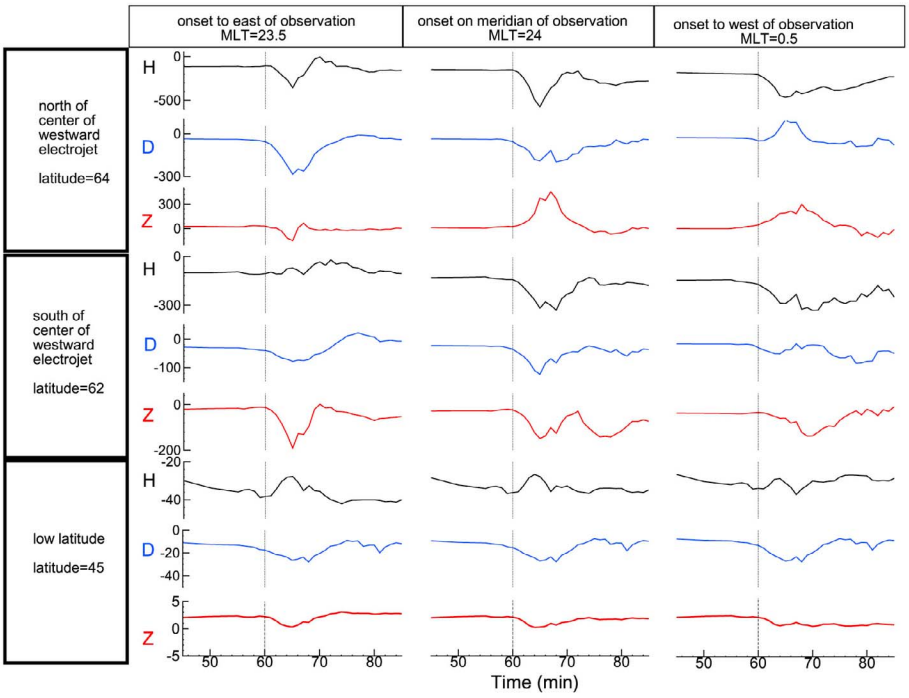

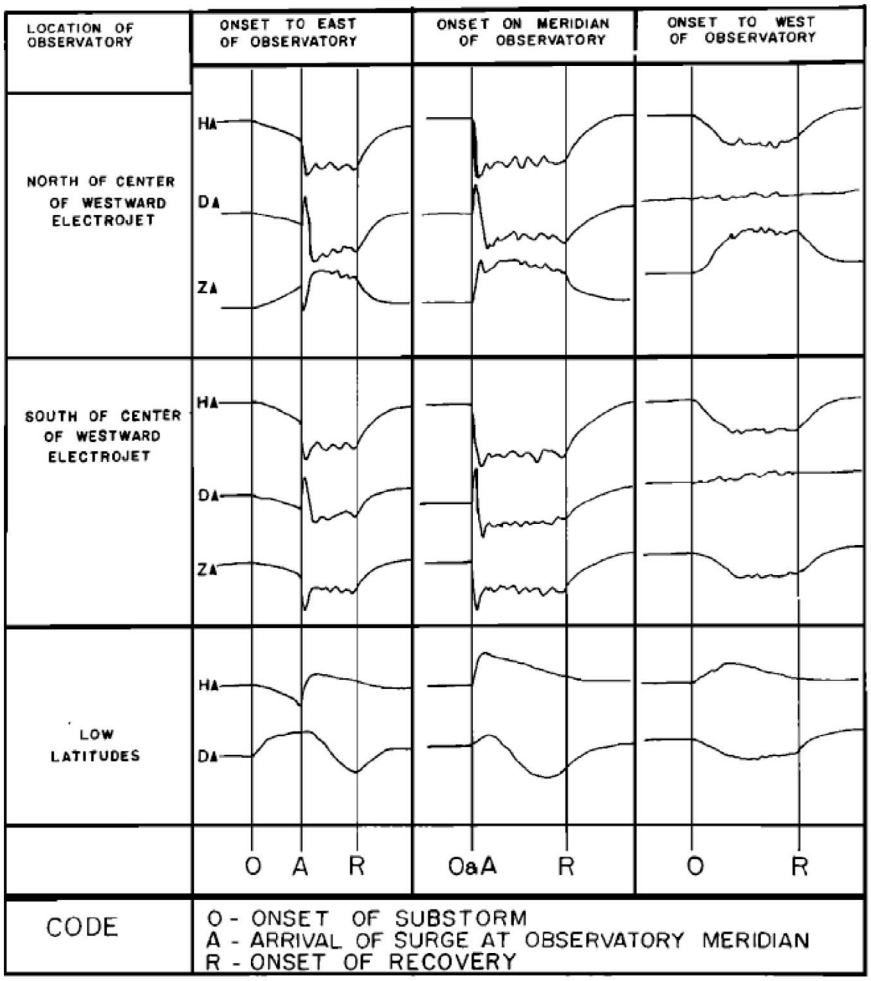

Figure 10. (top) The calculated ground magnetograms (H, northward in black; D, eastward in blue; Z, downward in red) at different locations during this idealized bubble injection event and (bottom) schematic results for typical substorms (adapted from *Rostoker et al.* [1980, Figure 1]).

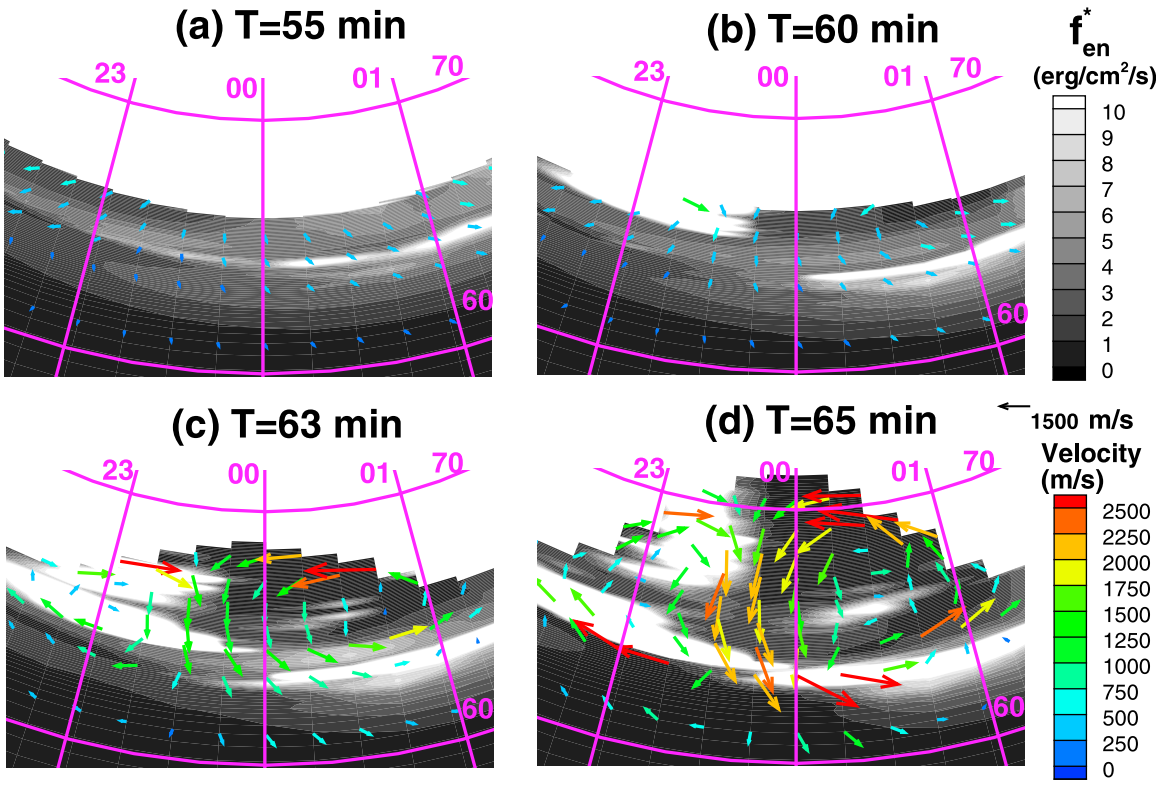

Figure 11. The modified precipitation energy flux f_{en}^{*} (gray scales, see equation (1) for definition) and ionospheric $\boldsymbol{E} \times \boldsymbol{B}$ drift velocity (colored arrows).

portion of the equatorward edge of the bubble mapped in the ionosphere. Its longitudinal extension is about half the width of the bubble.

[17] In order to compare our results with the classic ground magnetometer data during typical substorms [*Rostoker et al.*, 1980, Figure 1], we calculated the magnetograms at various locations relative to the center of the westward electrojet shown in Figure 10. The comparison is assessed only in a qualitative sense as the magnetogram map summarized by *Rostoker et al.* only depicts the schematic representation of ground magnetic field disturbance and our simulation is merely an idealized case. Consistency is found at most of the locations, including the indication of strong westward electrojet in the auroral zone and the positive excursion in H component in the low latitudes. There are two major differences from observations. First, the H component increases slightly at the location west and south of the center of the westward electrojet (the fourth curve from top in the left column), which is opposite to the changes at other high latitude locations. This is the signature of the Harang discontinuity. However, in the schematic map of *Rostoker et al.*, the feature of the Harang discontinuity is not seen, which is probably due to its relatively shorter time scale and smaller spatial scale than the Harang discontinuity during times other than substorm expansion phase (e.g., quiet times and substorm growth phase). Second, the D component shows a relatively large increase at the location east and north of the center of the westward electrojet (the second curve from top in the right column), which is due to a fairly strong southward component of the ionospheric currents around the footprint of the eastward edge of the bubble.

2.4. Ionospheric Flows and Precipitation Energy Flux

[18] In the current version of the RCM-E, the electron precipitation is assumed to be at 1/3 of the strong-pitch angle scattering limit in the plasma sheet, and parallel potential drops are set to zero, assumptions that seem appropriate for the diffuse aurora but not for more dynamic forms. Hence, we define a modified energy flux f_{en}^{*} in order to represent the electron precipitation energy flux more realistically:

$$f_{en}^{*} = f_{en}[1 + cJ_{FAC}^{up}/(qn_e\sqrt{k_B T_e/m_e})] \quad (1)$$

where f_{en} is the electron precipitation energy flux into the ionosphere computed assuming no auroral acceleration mechanism beyond adiabatic convection; c is a constant equal to 5; J_{FAC}^{up} is the upward FAC density (which is zero when current is downward); q is the electron charge, k_B is the Boltzmann constant, T_e, n_e and m_e are the electron temperature, number density and mass. The factor inside the parentheses represents the electron thermal current density. The term proportional to c qualitatively represents the acceleration due to the parallel electric field. The modified energy flux substantially exceeds f_{en} in regions where the upward FACs are strong compared with the electron thermal current.

[19] Figure 11a shows an east-west-aligned structure centered at ~64° latitude, which is presumably the diffuse aurora. The bright regions in Figures 11b, 11c and 11d experience a larger f_{en}^{*} than 11a, primarily due to the enhanced FACs. Besides the east-west-aligned structure, an additional bulge-like structure appears at higher latitudes,

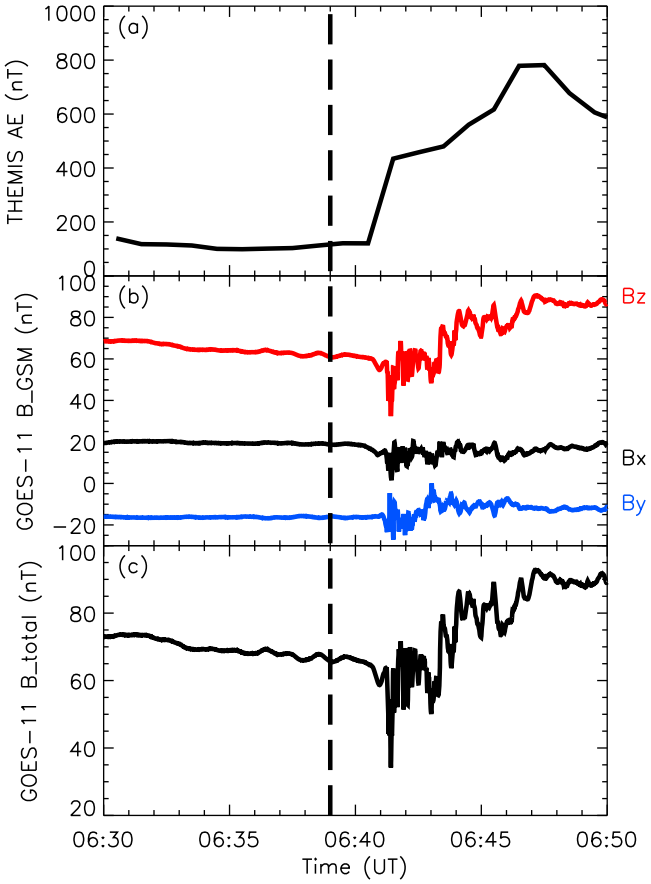

Figure 12. (a) THEMIS pseudo AE index, (b) magnetic field components in GSM and (c) total magnitude of magnetic field at GOES-11. The vertical line represents the onset time at ~06:39UT, April 9, 2008 identified by *Nishimura et al.* [2010], using ground ASI data.

corresponding to the large upward FAC density along the westward edge of the bubble. Again, the bulge starts its rapid poleward expansion at about T = 63 min, when the major dipolarization begins in the transition region at X ≈ −10 R_E. Figure 11 also shows that the plasma flows exhibit vortices centered at the edges of the footprints of the bubble, where the SCW is mostly intensified. Such vortex-like flow patterns have been observed in the plasma sheet [*Panov et al.*, 2010] and in the ionosphere [*Shi et al.*, 2012], and have also been reported in simulations [*Birn et al.* 2004; *Zhang et al.* 2009]. At the equatorward edge of the enhanced f_{en}^* layer, the plasma flows divert in the westward and eastward directions, poleward of which the flows are strongly equatorward inside the bubble channel, along the electric equipotentials (see black lines in Figure 9d). The reversals in plasma flows and electric fields are also referred to the electrically defined Harang reversal.

[20] The poleward expansion associated with bulge-like "aurora" requires further explanation. Throughout the simulation, the tailward boundary in the equatorial plane is fixed at $X = -15$ R_E at midnight. In the growth phase, the magnetic field is so stretched that the magnetic field maps from ~66° latitude in the ionosphere to X ~ −15 R_E in the magnetosphere. As the bubble is injected, the magnetic field dipolarizes strongly as a lot of magnetic flux is transported into the simulation region. Therefore, the magnetic field which mapped tailward of −15 R_E (or poleward of ~66° latitude) is now mapped earthward of the tailward boundary. Since the physics of electron acceleration and the excitation of auroral emission are not included in the RCM-E, which assumes zero field-aligned potential drops and no acceleration by kinetic Alfvén waves, the exact relationship between the actual poleward expansion of aurora in substorms and the poleward expansion of the enhanced f_{en}^* in our simulation require further investigation. However, if we assume that the main source for aurora emission is upward FACs (downward electrons), the bulge-like structure in the upward FACs is probably morphologically related to the auroral poleward expansion.

3. An Observational Example During a Deep Injection Event

[21] In this section, we will show a study of a real substorm event, in which a strong dipolarization is observed by GOES-11 in the magnetosphere during the expansion phase, along with the substantial intensification in the both region-1-sense and region-2-sense FACs inferred from ground magnetometer data. The onset of the substorm event occurred at ~06:39 UT, on April 9, 2008, identified by *Nishimura et al.* [2010] in the THEMIS all-sky-imager (ASI) data [*Mende et al.*, 2008; *Angelopoulos*, 2008]. The initial auroral brightening was recorded at FSMI station at MLAT 66° and MLT 21.7. Note that there were multiple substorm onsets which occurred on that day and we are analyzing the first one listed in "Data Set S2" in the work of *Nishimura et al.* [2010], which is not the one shown in their Figure 1.

[22] Figure 12 shows that the THEMIS pseudo AE index began to rise ~1.5 min after the auroral brightening from ~150 nT to nearly 800 nT within ~5 min. The GOES-11 spacecraft was at the same MLT as the substorm onset. Its magnetic field gradually weakened in the growth phase, and started to exhibit large-magnitude variations at ~06:41 UT, with a remarkable B_Z dip (a decrease of ~20 nT) followed by a substantial increase. The dipolarization became relatively stable after 06:47 UT, with a total amount of ~30 nT compared with the pre-onset level. The change of the B_Z component is very similar to our idealized simulation (Figure 3a), implying a typical bubble injection is detected at geosynchronous orbit. Furthermore, both the THEMIS D and E spacecraft observed magnetic field dipolarization, earthward flow and particle energization in the plasma sheet during the expansion phase at X~−8 and Y~8 R_E (not shown). Although a coordinated study using GOES and Geotail data by *Ohtani et al.* [2006] suggests that deep injection of fast flows into geosynchronous orbit is rare, as the north-south component of the magnetic field dipolarizes only in very few events within 15 min of the detection of fast flows, the event presented here shows evidence that it is an injection event penetrating deep into geosynchronous orbit.

[23] Estimated ionospheric current systems for this event are shown in Figure 13. The technique we used is the spherical elementary current systems (SECS) method developed by *Amm and Viljanen* [1999]. *Weygand et al.* [2011] have applied this method to estimate the horizontal and vertical current systems, over the North American Continent where ground magnetometer data from nearly 100

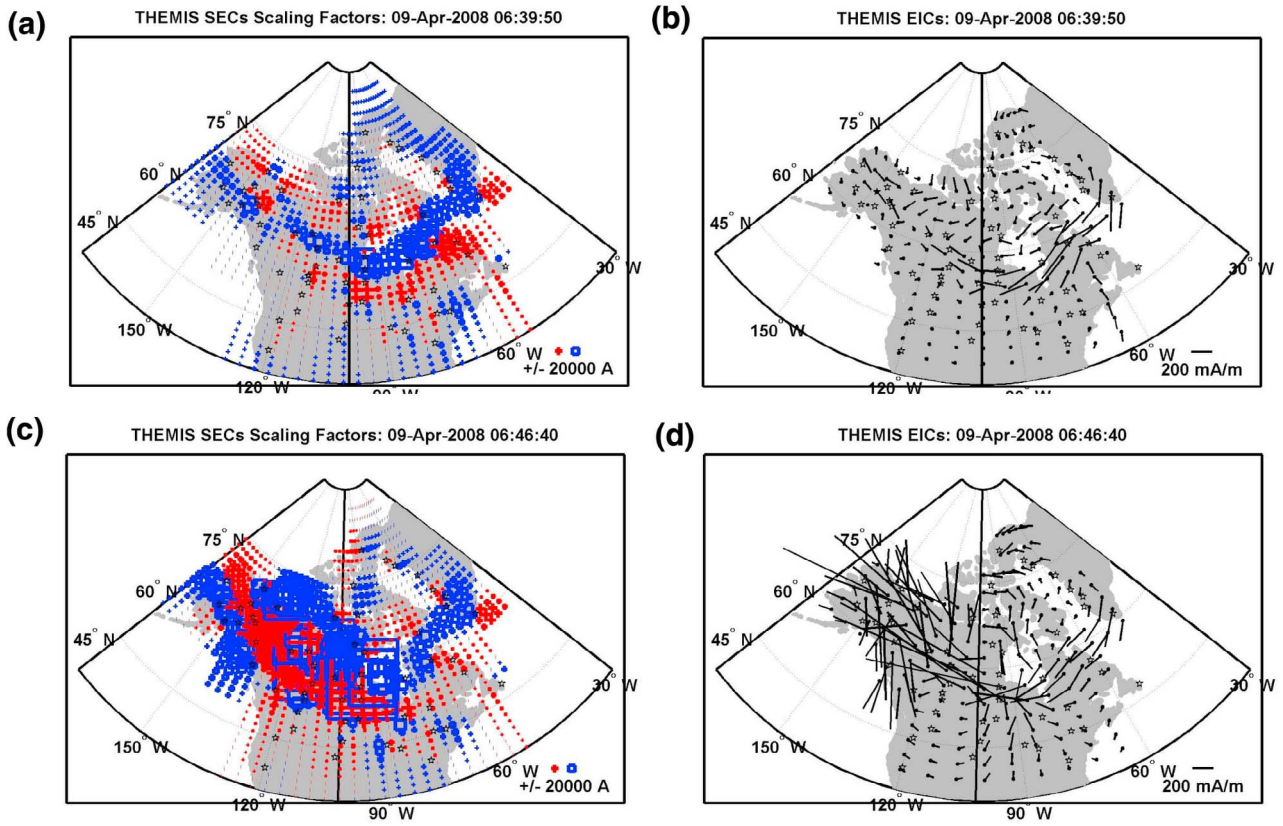

Figure 13. (left) The estimated elementary current amplitudes. The size indicates the magnitude of the current. The red and blue symbols represent the direction of vertical currents. (right) The estimated equivalent ionospheric currents. The length of the black vectors indicates the magnitude of the current. The top and bottom panels show the current systems around and after the substorm onset. The onset occurred at MLAT 66.0 and MLT 21.7 in the field of view of FSMI station at ~06:39UT, April 9, 2008 [*Nishimura et al.*, 2010].

stations are potentially available from 2007 to 2011. One can identify three major features that are consistent with the predictions of our simulation, by comparing the top row at 06:39:50 UT, a time that is near auroral onset but before the major dipolarization at GOES-11, with the bottom row at 06:46:40 UT, a time when the dipolarization and THEMIS pseudo AE index are near their maxima. First, two sets of intensified vertical current systems emerge and center around the onset location (Figure 13c), with the downward currents (blue) east of the upward currents (red) in the higher latitude region and the downward currents west of the upward currents in the lower latitude region. Second, the strong westward electrojet is reproduced with a latitudinal width of ~10° and longitudinal width of ~50°. Third, a clockwise vortex-like horizontal current system appears eastward of the onset sector.

4. Discussion and Conclusions

[24] We have described the large-scale current systems in both the magnetosphere and the ionosphere and their induced ground magnetic field disturbance during an idealized deep bubble injection event modeled with the RCM-E. We also estimated the horizontal and vertical current systems in and above the ionosphere for a real substorm event with a deep penetration flow burst. The simulation results and observations exhibit good qualitative agreement, considering the simulation was not originally designed for that event.

[25] The magnetospheric and the ionospheric dynamics are summarized in the cartoon of Figure 14. From the inner magnetospheric point of view, the driver of the reconfiguration is the fast earthward propagation of a bubble as represented by the depletion of plasma content through the tail boundary, which is created by either magnetic reconnection further down tail or other instabilities that can violate the frozen-in-flux condition [e.g., *Birn et al.*, 2009; *Yang et al.*, 2011b; *Hu et al.*, 2011]. In the magnetosphere (Figure 14, bottom), the bubble (pink), consisting of low entropy flux tubes, is injected earthward, as it partially disrupts the cross-tail current in the plasma sheet. The cross-tail current is then diverted via downward FACs into the ionosphere on the eastward side of the bubble and is connected to the upward FACs west of the bubble; this is essentially the substorm current wedge. The plasma ahead of the bubble is compressed (adiabatically in the context of the RCM-E) and is pushed earthward with the same speed as the bubble, resulting in a high entropy structure (amber) in which the magnetic field strength is reduced but the plasma pressure is enhanced. The bubble and the high entropy structure ahead of it are

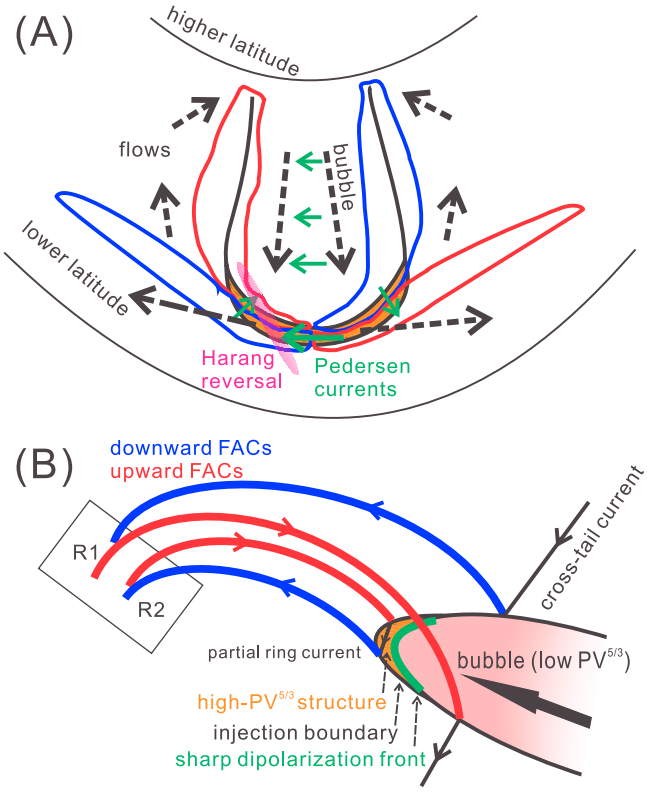

Figure 14. Cartoon of deep-bubble-injection-associated dynamics in (a) the nightside ionosphere (noon is at the top) and (b) the magnetosphere (the Sun is to the left).

separated by the dipolarization front (the green line) where the magnetic field strength increases sharply. Detailed study in Paper 1 also showed that the injection boundary for energetic particles consists of the most earthward boundary of the bubble and the high entropy structure (the black oval line). In the lower latitude region, an intensified region-2-sense FAC system forms and connects to the westward enhanced partial ring current near the equatorial plane. In the ionosphere (Figure 14, top), the footprints of the bubble are propagating equatorward. The region-1-sense FACs are on the western and eastern edges of the bubble and also extend equatorward along the poleward edge of the high entropy structure, while the intensified region-2-sense FACs are mapped on the equatorward edge of the high entropy structure. The green arrows indicate that the region-1-sense and the region-2-sense FACs are interconnected mainly by strong Pedersen currents. The induced plasma flows (dashed black arrows) show two vortex-like patterns centered on the edges of the bubble (which also appear in the magnetosphere, but not shown here). A Harang-reversal-like structure extends across the upward and downward FACs westward of the equatorward center of the bubble, which can be identified either in the flow directions or in the ground magnetic ΔH component. It is interesting to note that *Zou et al.* [2009b] analyzed data from radars, all-sky-imagers, and ground magnetometers for several substorm events, and that their description of the FACs, Pedersen currents and plasma flows in the ionosphere during the expansion phase is morphologically similar to our results (see Figure 14 of their paper). However, we also find that whether the flow shear around the Harang reversal strengthens or weakens near substorm onset may vary from case to case [*Zou et al.*, 2009a; *Bristow and Jensen*, 2007].

[26] We want to emphasize two notable features obtained from our simulation, which are closely related to the magnetic field mapping and thus the magnetic field modeling.

[27] 1. There are co-existing enhanced region-1-sense and region-2-sense FACs during the substorm injection, which are interconnected mainly by meridional Pedersen currents in the ionosphere. This feature has already been suggested in previous studies, though from different perspectives. *Untiedt and Baumjohann* [1993] referred this feature as the "Pedersen Loop." *Lui and Kamide* [2003] showed evidence of the dominance of a meridional current system during substorms which is presumably the Pedersen current in the ionosphere. A previous RCM simulation of a substorm injection that occurred on 22 July 1998 also shows the enhanced region-2-sense FACs accompanied with the SCW [*Zhang et al.*, 2009]. Understanding the two pairs of FACs is particularly important in terms of magnetic field modeling, because it suggests that the conventional SCW model is not the only FAC system during at least some substorms. Inclusion of the enhanced region-2-sense FACs as well as its connected partial ring current is needed. Recent studies by *Sergeev et al.* [2011] confirm that the magnetic field calculated by merely using a spread-out-wire-like SCW model exhibits substantial and systematic discrepancy with observations. They suggest that the discrepancy can be partially attributed to the lack of a module representing the intensified region-2-sense FACs.

[28] 2. The poleward expansion of the upward FACs to higher latitude exhibits a bulge-like structure that seems to be related to the poleward auroral expansion. Our simulation shows that the substantial poleward expansion is due to the dramatic change in the magnetic field mapping associated by the dipolarization, although the bulk flow of the associated equatorial plasma is earthward. We assume no specific mechanism for creating the bubble in the RCM-E, which suggests that the dipolarization itself, which is a well established feature of substorms, plays the key role in the poleward expansion, independent of the controversy about what microphysical processes are involved in causing the dipolarization. *Kubyshkina et al.* [2011] used an adaptive magnetic field model to mimic the stretching and dipolarization during a substorm event and drew a similar conclusion that the auroral poleward expansion is mostly due to the magnetic field mapping.

[29] In this paper, we only discussed the large-scale morphology of the calculated current systems, without providing a detailed quantitative description, because we realize that the model we used misses some physics which may affect the accuracy of our results. We list the following directions that are needed in the future study/improvement:

[30] 1. We should include inertial effects in the RCM-E. In the present RCM-E, the flows are assumed to be slow compared with MHD waves, though that is not always the case. The magnetic field is calculated by using a force equilibrium solver and the FACs are calculated by using the Vasyliunas equation, which may lead to larger FACs and

faster injection velocity than it should be during substorm expansions [*Wolf et al.*, 2012]. Thus, accurate calculation of the magnitude of the region-1-sense and region-2-sense FACs and their time scales for strengthening and decay require the inclusion of inertial effects.

[31] 2. The RCM-E needs to take account of the effects of non-adiabatic auroral acceleration mechanisms. During substorm onset and expansion phase, *Newell et al.* [2010] have shown that the particle acceleration above the ionosphere is closely related with both the Alfvénic aurora associated with wave activity and the monoenergetic aurora associated with quasi-static electric field during inverted-V events. The latter process requires the inclusion of parallel potential drops, using the *Knight* [1973] relation or a more elaborate model, which will allow us to investigate the relationship between the more realistic auroral morphology and the current systems.

[32] 3. More sophisticated models for electron and/or proton precipitation should be used. The strong pitch angle scattering assumption may be valid for the plasma sheet region, but is probably too simple for the region earthward of the inner edge of the plasma sheet. More accurate calculation of the ionospheric conductance is of particular importance to the investigation of the formation of the Harang reversal.

[33] 4. We must conduct more comprehensive simulations by varying different model inputs systematically. Although both *Ohtani et al.* [2004] and *Runov et al.* [2011] showed that the dipolarization front can be observed in a large portion of the plasma sheet, it is still unclear whether the two pairs of FACs, as well as the dipolarization front (see details in Paper 1), will appear simultaneously for all substorm injections, or whether they only emerge during certain conditions. It is physically clear that region-1-sense FACs must flow on the east and west sides of a bubble, which consist of dipolarized field lines. However, we speculate that the region-2-sense FACs may physically arise only when the bubble gets close to the transition region where the tailward gradient of $PV^{5/3}$ is fairly large [*Yang*, 2010]. The RCM-E inputs related to this question include (but may be not limited to) the value of $PV^{5/3}$ inside the bubble, the width of the bubble and the preconditioning during the growth phase.

[34] 5. In addition to the idealized event modeling, real event simulations with data-driven inputs are needed.

[35] **Acknowledgments.** We thank S. Mende for a useful conversation. The work at Rice was supported by NASA Heliophysics Theory grant NNX11AJ38G and NASA Guest Investigator grant NNX10AQ43G. The work by J. Y. was also supported by NSF AGS-1027208. We acknowledge NASA contract NAS5-02099 and V. Angelopoulos for use of data from the THEMIS Mission. We also thank H. Singer for providing GOES magnetic field data. J. M. Weygand was supported by NASA THEMIS grant SA3650 at UCLA. We would like to thank the many different magnetometer arrays for providing magnetometer data for this study including the Canadian Space Science Data Portal. The Canadian Space Science Data Portal is funded in part by the Canadian Space Agency, the Alberta Science and Research Authority, and the University of Alberta. The Canadian Magnetic Observatory Network (CANMON) is maintained and operated by the Geological Survey of Canada - http://gsc.nrcan.gc.ca/geomag. Magnetometer Array for Cusp and Cleft Studies (MACCS) array is supported by U.S. National Science Foundation grant ATM-0827903 to Augsburg College. We would like to thank the following: M. J. Engebretson, D. Murr, and E.S. Steinmetz at Augsburg College and the MACCS team. The Solar and Terrestrial Physics (STEP) magnetometer file storage is at Department of Earth and Planetary Physics, University of Tokyo and is maintained by K. Hayashi (hayashi@grl.s.u-tokyo.ac.jp).

[36] Robert Lysak thanks the reviewers for their assistance in evaluating this paper.

References

Akasofu, S.-I. (1964), The development of the auroral substorm, *Planet. Space Sci.*, *12*, 273–282, doi:10.1016/0032-0633(64)90151-5.

Akasofu, S. I., S. Chapman, and C. I. Meng (1965), The polar electrojet, *J. Atmos. Sol. Terr. Phys.*, *27*, 1275–1305, doi:10.1016/0021-9169(65)90087-5.

Amm, O., and A. Viljanen (1999), Ionospheric disturbance magnetic field continuation from the ground to the ionosphere using spherical elementary currents systems, *Earth Planets Space*, *51*, 431–440.

Angelopoulos, V. (2008), The THEMIS mission, *Space Sci. Rev.*, *141*, 5–34, doi:10.1007/s11214-008-9336-1.

Birn, J., J. Raeder, Y. L. Wang, R. A. Wolf, and M. Hesse (2004), On the propagation of bubbles in the geomagnetic tail, *Ann. Geophys.*, *22*, 1773–1786, doi:10.5194/angeo-22-1773-2004.

Birn, J., M. Hesse, K. Schindler, and S. Zaharia (2009), Role of entropy in magnetotail dynamics, *J. Geophys. Res.*, *114*, A00D03, doi:10.1029/2008JA014015.

Bristow, W. A., and P. Jensen (2007), A superposed epoch study of SuperDARN convection observations during substorms, *J. Geophys. Res.*, *112*, A06232, doi:10.1029/2006JA012049.

Chen, C.-K., R. A. Wolf, M. Harel, and J. L. Karty (1982), Theoretical Magnetograms Based on Quantitative Simulation of a Magnetospheric Substorm, *J. Geophys. Res.*, *87*(A8), 6137–6152, doi:10.1029/JA087iA08p06137.

Chen, C. X., and R. A. Wolf (1999), Theory of thin-filament motion in Earth's magnetotail and its application to bursty bulk flows, *J. Geophys. Res.*, *104*(A7), 14,613–14,626, doi:10.1029/1999JA900005.

Clauer, C. R., and R. L. McPherron (1974), Mapping the local time-universal time development of magnetospheric substorms using mid-latitude magnetic observations, *J. Geophys. Res.*, *79*(19), 2811–2820, doi:10.1029/JA079i019p02811.

Erickson, G. M., R. W. Spiro, and R. A. Wolf (1991), The physics of the Harang discontinuity, *J. Geophys. Res.*, *96*, 1633–1645, doi:10.1029/90JA02344.

Gkioulidou, M., C.-P. Wang, L. R. Lyons, and R. A. Wolf (2009), Formation of the Harang reversal and its dependence on plasma sheet conditions: Rice convection model simulations, *J. Geophys. Res.*, *114*, A07204, doi:10.1029/2008JA013955.

Harang, L. (1946), The mean field of disturbance of polar geomagnetic storms, *Terr. Magn. Atmos. Electr.*, *51*, 353–380, doi:10.1029/TE051i003p00353.

Harel, M., R. Wolf, R. Spiro, P. Reiff, C.-K. Chen, W. Burke, F. Rich, and M. Smiddy (1981), Quantitative Simulation of A Magnetospheric Substorm, 2. Comparison with Observations, *J. Geophys. Res.*, *86*(A4), 2242–2260, doi:10.1029/JA086iA04p02242.

Heppner, J. P. (1972), The Harang discontinuity in auroral belt ionospheric currents, *Geophys. Norv.*, *29*, 105–120.

Hesse, M., and J. Birn (1991), On Dipolarization and Its Relation to the Substorm Current Wedge, *J. Geophys. Res.*, *96*(A11), 19,417–19,426, doi:10.1029/91JA01953.

Hu, B., R. A. Wolf, F. R. Toffoletto, J. Yang, and J. Raeder (2011), Consequences of violation of frozen-in-flux: Evidence from OpenGGCM simulations, *J. Geophys. Res.*, *116*, A06223, doi:10.1029/2011JA016667.

Karty, J. L., R. A. Wolf, and R. W. Spiro (1984), Region one currents connecting to sunward convecting flux tubes, in *Magnetospheric Currents*, *Geophys. Monogr. Ser.*, vol. 28, edited by T. A. Potemra, pp. 269–275, AGU, Washington, D. C., doi:10.1029/GM028p0269.

Knight, S. (1973), Parallel electric fields, *Planet. Space Sci.*, *21*, 741–750, doi:10.1016/0032-0633(73)90093-7.

Kubyshkina, M., V. Sergeev, N. Tsyganenko, V. Angelopoulos, A. Runov, E. Donovan, H. Singer, U. Auster, and W. Baumjohann (2011), Time-dependent magnetospheric configuration and breakup mapping during a substorm, *J. Geophys. Res.*, *116*, A00I27, doi:10.1029/2010JA015882.

Lui, A. T. Y., and Y. Kamide (2003), A fresh perspective of the substorm current system and its dynamo, *Geophys. Res. Lett.*, *30*(18), 1958, doi:10.1029/2003GL017835.

McPherron, R. L., C. T. Russell, and M. P. Aubry (1973), 9. Phenomenological model for substorms, *J. Geophys. Res.*, *78*(16), 3131–3149, doi:10.1029/JA078i016p03131.

Mende, S. B., S. E. Harris, H. U. Frey, V. Angelopoulos, C. T. Russell, E. Donovan, B. Jackel, M. Greffen, and L. M. Peticolas (2008), The THEMIS array of ground-based observatories for the study of auroral substorms, *Space Sci. Rev.*, *141*, 357–387, doi:10.1007/s11214-008-9380-x.

Nagai, T. (1982), Observed Magnetic Substorm Signatures at Synchronous Altitude, *J. Geophys. Res.*, *87*(A6), 4405–4417, doi:10.1029/JA087iA06p04405.

Nakamura, R., et al. (2004), Spatial scale of high-speed flows in the plasma sheet observed by Cluster, *Geophys. Res. Lett.*, *31*, L09804, doi:10.1029/2004GL019558.

Newell, P. T., A. R. Lee, K. Liou, S.-I. Ohtani, T. Sotirelis, and S. Wing (2010), Substorm cycle dependence of various types of aurora, *J. Geophys. Res.*, *115*, A09226, doi:10.1029/2010JA015331.

Nishimura, Y., L. R. Lyons, S. Zou, V. Angelopoulos, and S. B. Mende (2010), Reply to comment by Harald U. Frey on "Substorm triggering by new plasma intrusion: THEMIS all-sky imager observations", *J. Geophys. Res.*, *115*, A12233, doi:10.1029/2010JA016182.

Ohtani, S., M. Shay, and T. Mukai (2004), The temporal structure of the fast plasma flow in the plasma sheet: Comparison between observations and two-fluid simulations, *J. Geophys. Res.*, *109*(A3), A03210, doi:10.1029/2003JA010002.

Ohtani, S., H. J. Singer, and T. Mukai (2006), Effects of the fast plasma sheet flow on the geosynchronous magnetic configuration: Geotail and GOES coordinated study, *J. Geophys. Res.*, *111*, A01204, doi:10.1029/2005JA011383.

Ontiveros, P. A. (2009), Synthetic magnetogram calculations from magnetosphere-ionosphere coupling models, Ph.D. dissertation, Rice Univ., Houston, Tex.

Panov, E. V., et al. (2010), Multiple overshoot and rebound of a bursty bulk flow, *Geophys. Res. Lett.*, *37*, L08103, doi:10.1029/2009GL041971.

Pontius, D. H., Jr., and R. A. Wolf (1990), Transient flux tubes in the terrestrial magnetosphere, *Geophys. Res. Lett.*, *17*, 49–52, doi:10.1029/GL017i001p00049.

Rostoker, G., S.-I. Akasofu, J. Foster, R. Greenwald, Y. Kamide, K. Kawasaki, A. Lui, R. McPherron, and C. Russell (1980), Magnetospheric Substorms-Definition and Signatures, *J. Geophys. Res.*, *85*(A4), 1663–1668, doi:10.1029/JA085iA04p01663.

Runov, A., V. Angelopoulos, M. I. Sitnov, V. A. Sergeev, J. Bonnell, J. P. McFadden, D. Larson, K.-H. Glassmeier, and U. Auster (2009), THEMIS observations of an earthward-propagating dipolarization front, *Geophys. Res. Lett.*, *36*, L14106, doi:10.1029/2009GL038980.

Runov, A., V. Angelopoulos, X.-Z. Zhou, X.-J. Zhang, S. Li, F. Plaschke, and J. Bonnell (2011), A THEMIS multicase study of dipolarization fronts in the magnetotail plasma sheet, *J. Geophys. Res.*, *116*, A05216, doi:10.1029/2010JA016316.

Sergeev, V. A., V. Angelopoulos, J. T. Gosling, C. A. Cattell, and C. T. Russell (1996), Detection of localized, plasma-depleted flux tubes or bubbles in the midtail plasma sheet, *J. Geophys. Res.*, *101*(A5), 10,817–10,826, doi:10.1029/96JA00460.

Sergeev, V. A., V. Angelopoulos, S. Apatenkov, J. Bonnell, R. Ergun, R. Nakamura, J. McFadden, D. Larson, and A. Runov (2009), Kinetic structure of the sharp injection/dipolarization front in the flow-braking region, *Geophys. Res. Lett.*, *36*, L21105, doi:10.1029/2009GL040658.

Sergeev, V. A., N. A. Tsyganenko, M. V. Smirnov, A. V. Nikolaev, H. J. Singer, and W. Baumjohann (2011), Magnetic effects of the substorm current wedge in a "spread-out wire" model and their comparison with ground, geosynchronous, and tail lobe data, *J. Geophys. Res.*, *116*, A07218, doi:10.1029/2011JA016471.

Shi, Y., E. Zesta, L. R. Lyons, J. Yang, A. Boudouridis, Y. S. Ge, J. M. Ruohoniemi, and S. Mende (2012), Two-dimensional ionospheric flow pattern associated with auroral streamers, *J. Geophys. Res.*, *117*, A02208, doi:10.1029/2011JA017110.

Song, Y., and R. Lysak (2001), Towards a new paradigm: From a quasi-static description to a dynamical description of the magnetosphere, *Space Sci. Rev.*, *95*, 273, doi:10.1023/A:1005288420253.

Southwood, D. J., and M. G. Kivelson (1991), An Approximate Description of Field-Aligned Currents in a Planetary Magnetic Field, *J. Geophys. Res.*, *96*(A1), 67–75, doi:10.1029/90JA01806.

Toffoletto, F. R., R. W. Spiro, R. A. Wolf, J. Birn, and M. Hesse (2000), Computer experiments on substorm growth and expansion, in *Proceedings of the 5th International Conference on Substorms*, ESA SP-443, edited by A. Wilson, pp. 351–355, Eur. Space Agency, Paris.

Toffoletto, F. R., S. Sazykin, R. Spiro, and R. Wolf (2003), Inner magnetospheric modeling with the Rice Convection Model, *Space Sci. Rev.*, *107*, 175–196, doi:10.1023/A:1025532008047.

Untiedt, J., and W. Baumjohann (1993), Studies of polar current systems using the IMS Scandinavian magnetometer array, *Space Sci. Rev.*, *63*, 245–390, doi:10.1007/BF00750770.

Vasyliunas, V. M. (1970), Mathematical models of magnetospheric convection and its coupling to the ionosphere, in *Particles and Fields in the Magnetosphere*, edited by B. M. McCormac, pp. 60–71, Springer, New York, doi:10.1007/978-94-010-3284-1_6.

Weygand, J. M., O. Amm, A. Viljanen, V. Angelopoulos, D. Murr, M. J. Engebretson, H. Gleisner, and I. Mann (2011), Application and validation of the spherical elementary currents systems technique for deriving ionospheric equivalent currents with the North American and Greenland ground magnetometer arrays, *J. Geophys. Res.*, *116*, A03305, doi:10.1029/2010JA016177.

Wolf, R. A., C. X. Chen, and F. R. Toffoletto (2012), Thin filament simulations for Earth's plasma sheet: Tests of validity of the quasi-static convection approximation, *J. Geophys. Res.*, *117*, A02216, doi:10.1029/2011JA016972.

Yang, J. (2010), Inner magnetospheric modeling during geomagnetic active times, Ph.D. dissertation, Rice Univ., Houston, Tex.

Yang, J., F. R. Toffoletto, and Y. Song (2010), Role of depleted flux tubes in steady magnetospheric convection: Results of RCM-E simulations, *J. Geophys. Res.*, *115*, A00I11, doi:10.1029/2010JA015731.

Yang, J., F. R. Toffoletto, R. A. Wolf, and S. Sazykin (2011a), RCM-E simulation of ion acceleration during an idealized plasma sheet bubble injection, *J. Geophys. Res.*, *116*, A05207, doi:10.1029/2010JA016346.

Yang, J., R. A. Wolf, and F. R. Toffoletto (2011b), Accelerated thinning of the near-Earth plasma sheet caused by a bubble-blob pair, *Geophys. Res. Lett.*, *38*, L01107, doi:10.1029/2010GL045993.

Yang, Y. S., R. W. Spiro, and R. A. Wolf (1994), Generation of region-1 current by magnetospheric pressure gradients, *J. Geophys. Res.*, *99*, 223–234, doi:10.1029/93JA02364.

Zhang, J.-C., R. A. Wolf, S. Sazykin, and F. R. Toffoletto (2008), Injection of a bubble into the inner magnetosphere, *Geophys. Res. Lett.*, *35*, L02110, doi:10.1029/2007GL032048.

Zhang, J.-C., R. A. Wolf, R. W. Spiro, G. M. Erickson, S. Sazykin, F. R. Toffoletto, and J. Yang (2009), Rice Convection Model simulation of the substorm associated injection of an observed plasma bubble into the inner magnetosphere: 2. Simulation results, *J. Geophys. Res.*, *114*, A08219, doi:10.1029/2009JA014131.

Zou, S., L. R. Lyons, C.-P. Wang, A. Boudouridis, J. M. Ruohoniemi, P. C. Anderson, P. L. Dyson, and J. C. Devlin (2009a), On the coupling between the Harang reversal evolution and substorm dynamics: A synthesis of SuperDARN, DMSP, and IMAGE observations, *J. Geophys. Res.*, *114*, A01205, doi:10.1029/2008JA013449.

Zou, S., L. R. Lyons, M. J. Nicolls, C. J. Heinselman, and S. B. Mende (2009b), Nightside ionospheric electrodynamics associated with substorms: PFISR and THEMIS ASI observations, *J. Geophys. Res.*, *114*, A12301, doi:10.1029/2009JA014259.

P. A. Ontiveros, Shell Exploration and Production Company, 150 N. Dairy Ashford, Houston, TX 77079, USA.

S. Sazykin, F. R. Toffoletto, R. A. Wolf, and J. Yang, Department of Physics and Astronomy, Rice University, MS 108, Houston, TX 77027, USA. (jianyang@rice.edu)

J. M. Weygand, Institute of Geophysics and Planetary Physics, University of California, 3845 Slichter Hall, PO Box 951567, Los Angeles, CA 90095, USA.